Direct Observation of Nanoscale Peltier and Joule Effects at Metal–Insulator Domain Walls in Vanadium Dioxide Nanobeams

Tela Favaloro,[†,‡,○] Joonki Suh,[§,○] Bjorn Vermeersch,[‡] Kai Liu,[§,∥] Yijia Gu,[⊥] Long-Qing Chen,[⊥] Kevin X. Wang,[§] Junqiao Wu,[§,∥] and Ali Shakouri*[,†,‡]

[†]Baskin School of Engineering, University of California, Santa Cruz, California 95064, United States

[‡]Birck Nanotechnology Center, Purdue University, West Lafayette, Indiana 47907, United States

[§]Department of Materials Science and Engineering, University of California, Berkeley, California 94720, United States

[∥]Materials Sciences Division, Lawrence Berkeley National Laboratory, Berkeley, California 94720, United States

[⊥]Deparment of Materials Sciences and Engineering, Pennsylvania State University, University Park, Pennsylvania 16802, United States

Ⓢ *Supporting Information*

ABSTRACT: The metal to insulator transition (MIT) of strongly correlated materials is subject to strong lattice coupling, which brings about the unique one-dimensional alignment of metal–insulator (M–I) domains along nanowires or nanobeams. Many studies have investigated the effects of stress on the MIT and hence the phase boundary, but few have directly examined the temperature profile across the metal–insulating interface. Here, we use thermoreflectance microscopy to create two-dimensional temperature maps of single-crystalline VO_2 nanobeams under external bias in the phase coexisting regime. We directly observe highly localized alternating Peltier heating and cooling as well as Joule heating concentrated at the M–I domain boundaries, indicating the significance of the domain walls and band offsets. Utilizing the thermoreflectance technique, we are able to elucidate strain accumulation along the nanobeam and distinguish between two insulating phases of VO_2 through detection of the opposite polarity of their respective thermoreflectance coefficients. Microelasticity theory was employed to predict favorable domain wall configurations, confirming the monoclinic phase identification.

KEYWORDS: Vanadium dioxide, thermoreflectance microscopy, Peltier effect, Joule heating, metal–insulator domain wall
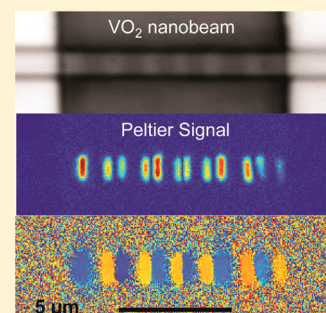
Strongly correlated materials share a unique feature where phase transitions result in significant changes in physical properties, making these materials of particular interest for their potential device applications beyond the scope of current semiconductor technologies. Such devices are inherently complicated in nature owing to strong coupling of the crystal lattice with charge, spin, and orbital degrees of freedom of electrons. Vanadium dioxide (VO_2) is one of such materials, extensively studied as it undergoes a highly stable high-temperature metal to low-temperature insulator transition (MIT) at $T_{MIT\text{-}Bulk} \approx 340$ K.[1] The electronic phase transition is accompanied by a structural transition in which a metallic rutile phase (M_R) converts to a semiconducting monoclinic phase (I),[2] resulting in ~1% expansion of the lattice along the tetragonal c-axis (C_R).[3,4] Multiple monoclinic lattice structures (I_{M1}, I_{M2}) are available for the insulating phase, which are almost optically identical and have very similar free energies,[5] adding to the complexity of the material system. The more resistive I_{M2} phase has a lattice constant ~0.6% longer[3] along C_R than I_{M1} and can act as an intermediate state between I_{M1} and M_R, generally associated with higher tensile strains.[6–10]

One-dimensionally aligned metal–insulator (M–I) domain configurations can be attained either by substrate-induced uniaxial strain[11–13] or nonuniform transition metal doping in a single-crystalline VO_2 nanobeam (NB).[14] In the former case, M_R domains appear gradually upon heating, shifting T_{MIT} depending on the nature of external stress. Given a strong adhesive interaction with the substrate, I_{M2} phase (with longer lattice constant along C_R) becomes thermodynamically stable and the alternating M–I heterostructures are spontaneously organized (Figure 1a). This substrate-mediated MIT leads to a gradual decrease in electrical resistance until VO_2 NB becomes fully metallic around ~390 K (Figure 1b). Though it is generally believed that the MIT is induced by the symmetric splitting of the t_{2g} band composed of 3d vanadium states[15] (Figure 1c), the physical nature of M–I wall is still undetermined and poorly understood despite its promising electrical and thermal applications at the nanometer scale.

In this letter, we investigate the electro-thermal activities at M–I walls by utilizing thermoreflectance imaging microscopy to create a thermal map of VO_2 NBs under current bias in the M–I coexisting phase regime. Thus far, electrical measurements
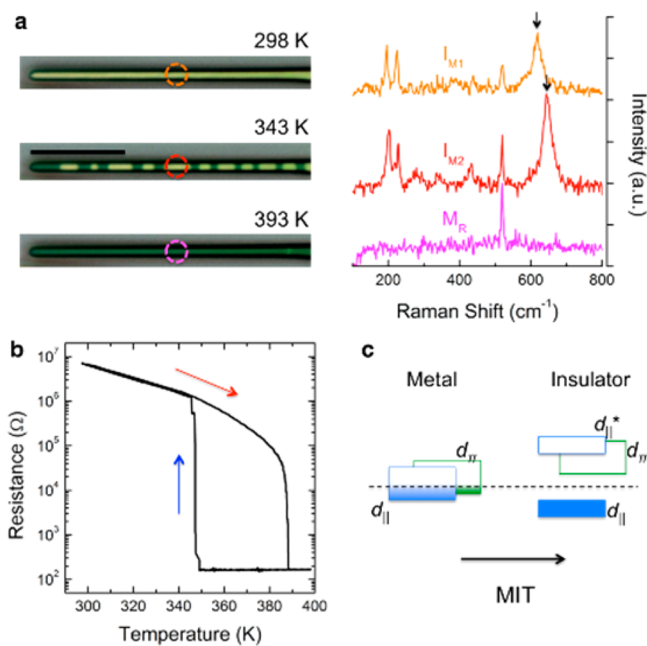
Figure 1. Metal−insulator heterostructures along an individual VO_2 nanobeam. (a) Optical images of a typical VO_2 NB upon heating from room temperature (I_{M1}) through coexisting domains (M_R and I_{M2}) to a fully metal M_R state. The physical domains are identified by Raman spectroscopy. Scale bar represents 10 μm. (b) Heating and cooling resistance as a function of temperature for device 1. (c) Band diagram for M and I phases.

of the thermoelectric properties of VO_2 NBs have been conducted over the length of the device,[16,17] determining effective material properties with indirect information about the domain interface. We report the direct observation of the highly localized Peltier cooling/heating and Joule heating at the M−I boundary, which acts as a thermal point source. In addition, our analysis suggests that an observed change in polarity of thermoreflectance coefficient can differentiate between the I_{M1} and I_{M2} insulating phases while our calculation of the microelastic strain on the NB M−I interface establishes each

monoclinic phase to have a unique and favorable domain wall configuration. These experiments provide insight into the native M−I heterostructures of VO_2 NBs. The M−I domain walls are expected to be truly nanometer-thick, suggesting exotic functionalities at the truly nanometer length scale.

The VO_2 NBs employed in this study were synthesized on 1 μm thick thermally grown SiO_2/Si substrates via a vapor transport approach.[18] These single-crystalline NBs varied in length from 20 to 250 μm and typically had a 0.5 μm^2 rectangular cross-section. Optically clean NBs were preselected, and then devices were fabricated by conventional photo-lithography with two or four Au/Cr contacts deposited with 10 μm spacing using e-beam evaporation. Rapid thermal annealing at 525 K for 2 min was subsequently applied to achieve ohmic contact; negligible contact resistance was confirmed by a comparison of four-probe and two-probe I−V measurements. VO_2 NBs are naturally bonded to the SiO_2/Si substrate and experience uniaxial tensile strain along C_R (oriented as the NB long axis) as a result of high temperature growth and thermal expansion mismatch between the NB and the substrate.

We have visualized the thermal response of NB devices to electrical bias using charge-coupled device (CCD)-based thermoreflectance thermal microscopy. This noninvasive method provides two-dimensional thermal images of a sample surface with 200−300 nm spatial and 10 mK temperature resolutions.[19] The technique relies on the small but detectable variation of the surface reflectivity with temperature, as quantified by the thermoreflectance coefficient C_{TR}, a material and illumination wavelength-dependent parameter[20] that defines the relationship between the relative reflectivity change $\Delta R/R$ to the thermal field ΔT (relative to ambient) at the device surface: $\Delta T = (1/C_{TR})(\Delta R/R)$.

In the following experiments, we used a narrowband green LED ($\lambda \approx 530$ nm) to illuminate the VO_2 NBs through a microscope objective with ×250 magnification and monitored the reflectivity of the NBs with a scientific grade CCD camera. Green illumination selected since the C_{TR} for the contact material (Au) is well-known at this wavelength.[21] The thermal images presented in this letter assume a uniform C_{TR} of -2×10^{-4} K^{-1}. The NB substrate was mounted with a thin layer of
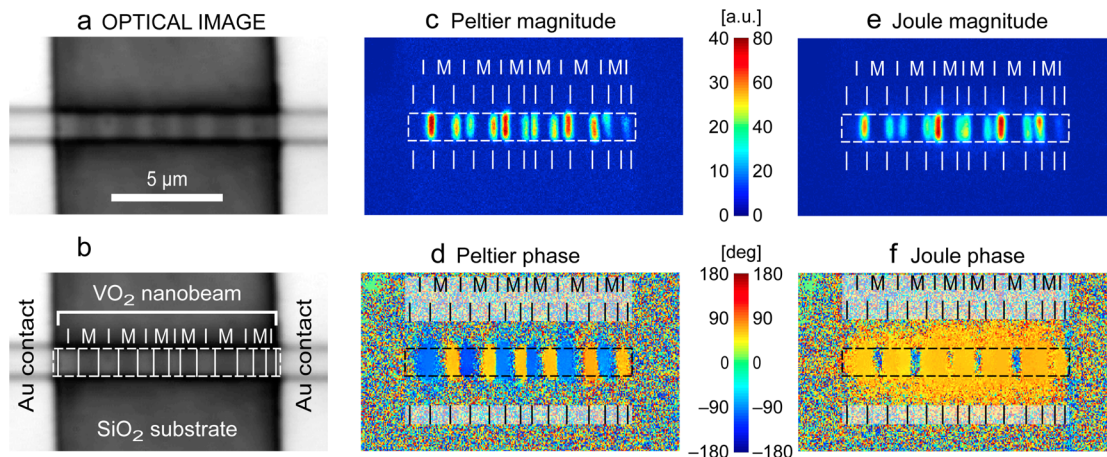

Figure 2. Thermoreflectance thermal images of device 1 taken at 355 K under 10 μA applied current. (a,b) Optical images of the nanobeam (greyscale). (c,d) Peltier temperature magnitude and phase images, respectively. (e,f) Joule temperature magnitude and phase images. While both Peltier and Joule signals are localized at the interfaces, phase images show very different dynamics of how alternating Peltier cooling and heating in nearby interfaces exchange energy mainly through the nanobeam. However, there is no cancellation in the Joule activity, and Joule heating is propagating in the substrate.
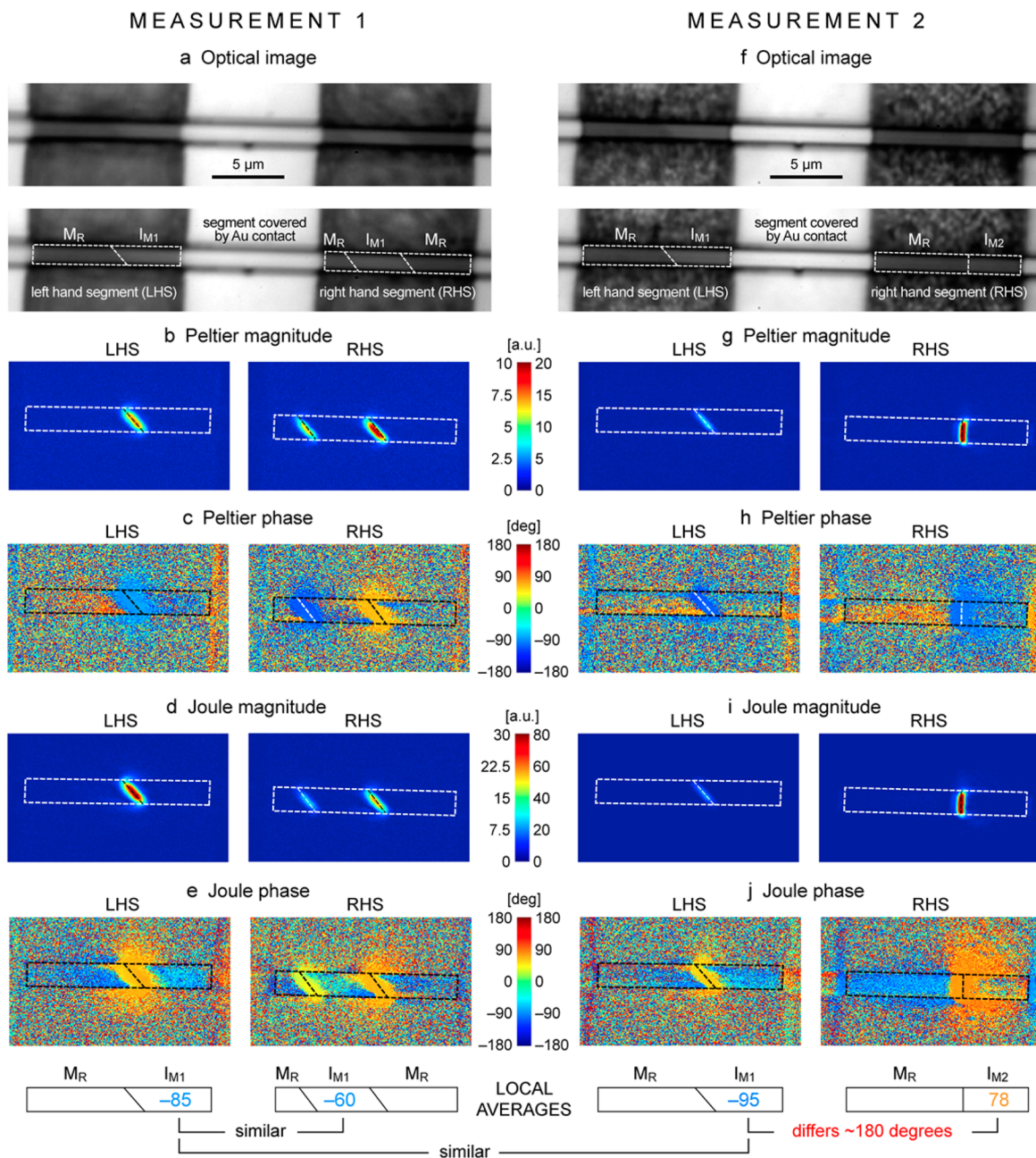
Figure 3. Thermal images of nonperiodic nanobeam (device 2) at 348 K under 8 μA current excitation. Two NB segments and the adjoining electrode region are under current bias. (a−e) Initial thermoreflectance measurement images of device 2 before the RHS segment changed from M−I−M to M−I domain configuration. (f−j) Thermal images for the same current bias taken after the RHS segment stabilized. As domain walls are at substantial distances from each other, both Joule and Peltier phase images show heat exchange mainly with the substrate. Also note the change in the phase of the Joule heating in the RHS segment, which is an indication of different thermoreflectance coefficient for the two insulating phases.

thermal paste onto a Peltier heater for ambient temperature control. We then applied a 3.75 Hz sinusoidal voltage across (multiple) segments of the NB to create a slowly oscillating thermal field. The bias period was several orders of magnitude longer than the typical thermal response times of devices this size, ensuring that the NBs were operating in the quasi-static thermal regime. Bias current amplitudes were limited to ∼15 μA such that the NB domains were not displaced by electro-thermal effects[22] in the M−I coexisting state. We employed the minimum possible current bias that induced a measurable signal while remaining in the linear regime of the I−V curve for the NB. We continuously monitored the optical image during the

measurement to ensure the stable configuration of M−I heterostructures along NBs.

The phase-locked CCD captured a periodic sequence of 8 images corresponding to eighth-period integrals of the reflectance signal under sinusoidal excitation. Data were averaged over ∼500 periodic cycles to achieve sufficient signal-to-noise ratios. Adequate mathematical processing provided the magnitude and relative phase of the first and second harmonic components of the reflectivity field.[23] This corresponds to a separation of the Peltier and Joule terms in the thermal field, given their respective linear (first harmonic) and quadratic (second harmonic) current dependencies. More detailed information regarding this technique including a

diagram of the experimental setup may be found in the Supporting Information (see also refs 23 and 24).

Several NBs were examined in this manner, and it became apparent that each NB could be categorized into one of two observed trends depending on the strength of the attachment to the substrate (hence built-in strain): the first type exhibited periodic domain configuration and had a smooth decrease in resistance with temperature as described in Figure 1. The second type of NB displayed few and irregular domain formation, accompanied by a distinct jump in electrical resistance around T_{MIT}. For clarity, representative examples of each category, designated device 1 and device 2, respectively, are analyzed in this letter.

We first present results for a VO$_2$ NB (device 1), which exhibited the typical periodic domain configuration; Raman spectroscopy (Figure 1a) established this device was in the M$_R$–I$_{M2}$ phase coexisting state.[10,25,26] Thermal images of the NB taken at 355 K under an applied 10 μA sinusoidal current are presented in Figure 2. As discussed, periodic domains are indicative of homogeneous substrate adhesion and are clearly observed in the optical image depicted in Figure 2a,b (greyscale image); this domain configuration remained stationary for the duration of the thermoreflectance measurement. Figure 2c,e displays the temperature magnitudes of the Peltier and Joule signals, respectively. Both signals originate in the interface regions between metal and insulator domains, which behave as thermal point sources. We expect to see Peltier heating or cooling at the M−I junction given the presence of an energy barrier.[27,16] In this case, the signal may not be fully resolvable in an optical measurement due to the diffraction limit. However, Joule heating is also concentrated at the M−I junction indicative of a significant resistance of the domain wall (R_{DW}) between the metallic and insulating domains. For the specific current amplitude depicted in these figures, Joule heating is stronger than the magnitude of Peltier and is consequently better resolved; the average ratio of the Joule magnitude to that of Peltier (J/P) is ∼1.75. It is interesting to note that while R_{DW} plays a minor role from an electrical standpoint (relative to the overall NB resistance), it is crucial from the perspective of the local thermal behavior of the NB. Thermal imaging reveals that the associated resistance is comprised in a very small region, leading to power densities at the M−I junction that are much higher than that along the length of the NB. Highly localized Joule heating may also be attributed to the band offset between M and I domains through the possible introduction of an associated depletion region; however, the exact nature of the junction is still unknown.

Phase information from the thermal signal can be much more revealing as it is quite sensitive to small variations in the thermal distribution across the sample. The thermal response time of the NB is approximately 5 orders of magnitude shorter than the period of the applied current, leading to uniform thermal phase. Thus, any deviations in the phase image are due to bipolar behavior (cooling instead of heating) or sign changes in the C_{TR}. The Peltier phase image (Figure 2d) depicts both heating and cooling localized at the M−I interfaces: when one interface is heating (under forward bias), the neighboring interface is clearly cooling (under reverse bias) denoted by the 180° phase shift. As expected, the Joule signal (Figure 2f) does not exhibit this phase shift and is always heating.

While the Peltier signal is seemingly concentrated inside the insulating region, we expect the actual thermal activity to also present in the metal region. We attribute the apparent lack of

thermal signal over the metallic state to a small thermoreflectance coefficient, as the images are based on a uniform C_{TR} calibrated for Au only. Phase-shifted Joule activity is evident in the metal regions of the NB and into the substrate owing to its stronger signal but is not visible in the magnitude images. To explain this result, the C_{TR} of the metal phase must be of opposite sign and significantly smaller in magnitude than that of the insulating state. It is evident in Figure 2f that the supporting substrate of the sample also functions as a heat sink for Joule heating. The signal spreads outward uniformly from its peak at the domain walls, demonstrating good thermal contact between the NB and the substrate. The lack of Peltier substrate activity is not simply because of its lesser signal magnitude. Heating and cooling signals at nearby domain walls are mainly coupled through the nanobeam with little leakage into the substrate; this interaction may diminish the overall Peltier magnitude in this device. Through inspection of the phase images, we can confirm that the resultant reflectivity signals are due to thermal fluctuations and not movement at the domain boundaries. The uniform thermal signals at the interfaces occur over a larger width than expected for edge effects from movement not observed optically. In addition, the point source-like behavior with continuous activity into other regions of the image (nearby substrate) would not be possible.

The apparent total strain (and thus domain pattern) differed between samples due to nonuniform substrate adhesion, variations in growth temperature, and stress induced by the end-to-end clamping by the contacts. In this sense, NBs with a nonperiodic M−I domain pattern are possible and display quite different temperature-dependent behavior, as is shown in Figure 3 for a sample (device 2) held at 348 K. Current was applied across two consecutive segments of the NB (Figure 3a,f); referred to in this letter as the right-hand side (RHS) segment and the left-hand side (LHS) segment. Irregular domain patterns nucleated from the side contacts at 328 K, a much lower ambient temperature as compared to device 1 and considering $T_{MIT-Bulk}$. The domain walls in both segments were initially at a ∼50° angle relative to the NB long axis. The domain configuration and angled domain walls of this NB can be indicative of nonuniform stress distribution along the length and width of the NB,[8,12,13] suggesting weak substrate interaction and/or clamping strain from the Au contacts.

For the thermoreflectance measurement, we applied sinusoidal current at varying amplitudes, ranging from 5 to 10 μA, very similar in magnitude to the previous NB as this was the minimum necessary to resolve the Peltier signal. After one measurement run at 8 μA bias, the domain configuration on the RHS changed from M−I−M with angled domain walls (Figure 3a−e) to M−I with a single vertical wall (Figure 3f−j), possibly due to excessive Joule heating at the interface. The new domain configuration was stable for all subsequent measurements.

The magnitude of Peltier temperature in the RHS segment was very similar to that of uniformly clamped NB (Figure 2c); however, Joule heating was substantially greater. For the same current bias applied for device 1 (10 μA), J/P$_{RHS}$ ≈ 7 and J/P$_{LHS}$ ≈ 5. Such significant Joule heating, especially on the RHS, could drive the domains to another insulating state (from I$_{M1}$ to I$_{M2}$). These highly localized junction Peltier and Joule effects are also responsible for M−I domain wall propagation along the VO$_2$ NBs at high currents (well above those used during the measurement), as previously reported in suspended W$_x$V$_{1−x}$O$_2$ NBs.[22] This is especially true for device 2, as the NB does not dissipate Joule heating well into the substrate possibly due to

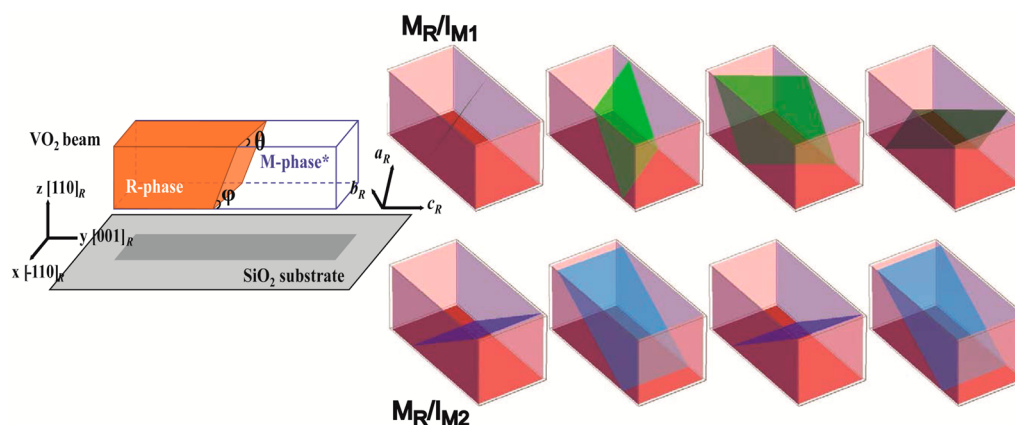**Figure 4.** Three-dimensional plots of possible habit planes for $\theta = 56°$ M_R/I_{M1} (green) and $\theta = 89°$ M_R/I_{M2} (blue). These habit planes exhibit minimized total elastic energy for the interface and are thus considered favorable.

weaker adhesion. The resultant phase oscillation could be controlled and sustained with the addition of a parallel capacitor by repeating the charging and discharging process (see Supporting Information).

The phase images of both Peltier (Figure 3c,h) and Joule (Figure 3e,j) confirm the earlier premise that the signals occur at the domain walls. The typical spreading pattern from a thermal point source is detected along the NB and into the substrate. The relative signal strengths along the NB show heat diffuses preferentially in the metal region of the RHS segment, possibly owing to its higher thermal conductivity.[28] Activity along the Au-covered-NB region gives us a reference value for C_{TR}, as this is known to be negative for Au at this illumination wavelength. From this and the expected uniformity of the Joule phase activity, we gain valuable insight about C_{TR} of the other regions. C_{TR} of the metal domains is always positive, while the C_{TR} of the insulator domain on the RHS segment of measurement 2 is negative (Figure 3j, RHS), similar to the scenario presented for device 1 in Figure 2. However, the insulating state in the LHS segment during the same measurement is roughly 180° out of phase from the aforementioned insulator domains, implying a positive C_{TR} (Figure 3j, LHS). We believe that the difference in the sign of C_{TR} between these two insulating domains distinguishes the two monoclinic phases of VO$_2$; that is, the reflectivity dependence on temperature variations has the opposite behavior for the two monoclinic states. This is in agreement with the phase information for the RHS segment before the change to the single vertical domain wall; the insulator domain on the RHS during measurement 1 (Figure 3e) is roughly 180° phase shifted from the I domain in the RHS during measurement 2 (Figure 3j) for the same excitation bias. For clarity, the average phase values of the NB regions associated with this analysis are presented below the phase images in Figure 3e,j. The significant change in the thermoreflectance properties between the two insulating phases could be attributed to the difference in reflective signatures of the two monoclinic phases under polarized light.[6,26,29] Further thermoreflectance measurements using a polarized light source would illuminate the underlying mechanism of the C_{TR} sign change.

We applied Khachaturyan's microelasticity theory for a single coherent inclusion in the matrix of a parent phase[30] to analyze the elastic energy and thus orientation of the M–I interface of a VO$_2$ NB in an attempt to understand the change in domain

wall alignment. Both the M_R/I_{M1} and M_R/I_{M2} junctions are considered coherent. As shown in our previous work,[31] both rutile–monoclinic structural transitions have four possible variants each with different stress-free transformation strains, leading to eight possible domain wall configurations all with minimized elastic energy density. The favored orientation exhibits reduced total elastic energy, which is related to the geometry of NB; accordingly, M_R/I_{M1} will favor an acute angle of 56° (Figure 4) with the NB top surface, while M_R/I_{M2} may display an 89° (Figure 4) or 33° acute angle. This is consistent with the experimentally observed angles of devices 1 and 2 whose insulating states are identified through the sign of C_{TR} during thermoreflectance imaging: the M_R/I_{M1} domain wall exhibits an angle of 48−52° and M_R/I_{M2} presents as a 90° interface (Figures 2 and 3). More details on the calculation of domain wall configurations can be found in the Supporting Information.

Further evidence identifying the insulating phases of device 1 and 2 is obtained by examining the resistance trend with ambient temperature of the two NBs (Figure 5). Device 2 exhibits a large jump in resistance at 335 K, coinciding with the appearance of the first metal domain. This implies that either R_{DW} is quite large, ~300 kΩ, or that I_{M1} converted to the more resistive I_{M2} insulating state, similar to the behavior described in Kasirga et al.[9] In contrast, device 1 shows a fairly steady decrease in resistance before becoming fully metallic. Both NBs
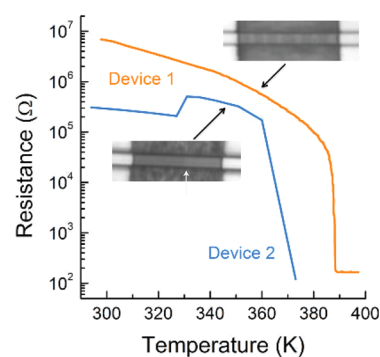

Figure 5. Resistance as a function of ambient temperature comparison of the two NBs: devices 1 and 2. Device 2 exhibits a jump in resistance coincident with the emergence of metallic domains due to the conversion from I_{M1} to I_{M2} and the additional resistance of the domain walls.

display the expected Arrhenius behavior for a nondegenerately doped semiconductor before the metal domains emerge, $R_I(T) = R_{I,0}\, e^{E_a/k_BT}$. However, device 2 has a markedly lower overall resistance despite similar sample geometries; thus, the two NBs have quite dissimilar activation energy: $E_{a(dev1)}$ = 0.3 eV and $E_{a(dev2)}$ = 0.11 eV; both are consistent with values reported in the literature ranging from 0.08 to 0.36 eV.[27,29,32,33] The lower activation energy suggests device 2 to be more highly doped. When the domains coexist, the total resistance R_T of the NB is composed of four factors:

$$R_T(T) = x(T)R_I(T) + [1 - x(T)]R_M(T) + R_C + R_{DW}$$

where $x(T)$ is the length fraction of the NB in the I state at a given ambient temperature, and R_I and R_M are the expected insulating and metal resistances, respectively. The contact resistance, R_C, was shown to be negligible. We used this equation and the extrapolated Arrhenius fitting at multiple ambient temperatures to determine R_{DW} of the more uniform NB (device 1), which we found to be 39 ± 7 kΩ. This value is in agreement with the figure put forth in Wei et al.[32]

The jump in resistance, sign change of the C_{TR}, and transformation of the interface angle of device 2 denote the change in monoclinic crystal structure in the M−I coexisting state. $T_{MIT-dev2}$ is a lower temperature than $T_{MIT-Bulk}$, indicating compressive strain driving the NB to the phases with smaller lattice constants (M_R and I_{M1}). The irregular domain patterns in addition to strong Joule activity at the M−I interface suggest poor substrate bonding, which would reduce tensile stress felt by the NB upon cooling from the high growth temperature (~1000 °C). Thus, device 2 was initially in the I_{M1} state. At elevated temperatures, the appearance of metal domains alleviates compressive strain while inducing tensile strain in the adjacent insulating domain. The induced strain, accompanied by intense Joule heating in the RHS segment generated by the current applied during the measurement, stimulated the conversion from I_{M1} phase to I_{M2}.

VO$_2$ NBs with good substrate adhesion would experience tensile strain at the temperatures of this experiment. Homogenous periodicity and uniform thermal signal in the substrate demonstrate uniaxial tensile strain in device 1 along the NB long axis, fixing the insulating phase to the I_{M2} phase with a longer lattice constant. The higher overall resistance and the persistence of I domains with vertical interfaces to 390 K, well above $T_{MIT-Bulk}$, further support this assertion. The sign of the C_{TR} of the I phase in device 1 is negative and is therefore I_{M2}, in agreement with the analysis of device 2 and confirmed by Raman spectroscopy.

In conclusion, our results directly reveal the extremely local Peltier and Joule effects across the M−I domain walls. Thermal images show that alternating Peltier heating and cooling at neighboring domain interfaces exchange energy through the nanobeam; while Joule heating dissipates in the substrate. We show that significant domain wall resistance is responsible for concentrated Joule heating. The insight gained through thermoreflectance imaging and the ability to distinguish between insulating phases illuminate the underlying impact of stress on the nanobeam, while examination of the elastic energy at the interface determines the favored wall configurations to minimize the total elastic strain for each monoclinic phase.

■ ASSOCIATED CONTENT

Ⓢ Supporting Information

Detailed methods and figures describe thermoreflectance microscopy technique. Supporting Information regarding the theoretical calculation of the elastic energy and domain wall oscillation at high applied currents are also provided. This material is available free of charge via the Internet at http://pubs.acs.org.

■ AUTHOR INFORMATION

Corresponding Author

*(A.S.) E-mail: shakouri@purdue.edu.

Author Contributions

○These authors (T.F. and J.S.) contributed equally to this work.

Notes

The authors declare no competing financial interest.

■ ACKNOWLEDGMENTS

■ REFERENCES

(1) Morin, F. J. *Phys. Rev. Lett.* **1959**, *3*, 34−36.

(2) Goodenough, J. B. *Phys. Rev.* **1960**, *117*, 1442.

(3) Marezio, M.; McWhan, D. B.; Remeika, J. P.; Dernier, P. D. *Phys. Rev. B* **1972**, *5*, 2541−2551.

(4) Rakotoniaina, J. C.; Mokrani-Tamiellin, R.; Gavarri, J. R.; Vacquier, G.; Cassalot, A.; Calcarin, G. *J. Solid State Chem.* **1993**, *103*, 81−94.

(5) Pouget, J. P.; Launois, H.; D'Haenens, J. P.; Merenda, P.; Rice, T. M. *Phys. Rev. Lett.* **1975**, *35*, 873−875.

(6) Cao, J.; Gu, Y.; Fan, W.; Chen, L. Q.; Ogletree, D. F.; Chen, K.; Tamura, N.; Kunz, M.; Barrett, C.; Seidel, J.; Wu, J. *Nano Lett.* **2010**, *10*, 2667−2673.

(7) Jones, A. C.; Berweger, S.; Wei, J.; Cobden, D.; Raschke, M. B. *Nano Lett.* **2010**, *10*, 1574−1581.

(8) Atkin, J. M.; Berweger, S.; Chavez, E. K.; Raschke, M. B.; Cao, J.; Fan, W.; Wu, J. *Phys. Rev. B* **2012**, *85*, 020101.

(9) Kasirga, T. S.; Sun, D.; Park, J. H.; Coy, J. M.; Fei, Z.; Xu, X.; Cobden, D. H. *Nat. Nanotechnol.* **2012**, *7*, 723−727.

(10) Zhang, S.; Chou, Y. C.; Lauhon, L. J. *Nano Lett.* **2009**, *9*, 4527−4532.

(11) Lopez, R.; Boatner, L. A.; Haynes, T. E.; Haglund, R. F.; Feldman, L. C. *Appl. Phys. Lett.* **2001**, *79*, 3161−3163.

(12) Wu, J. Q.; Gu, Q.; Guiton, B. S.; deLeon, N. P.; Ouyan, L.; Park, H. *Nano Lett.* **2006**, *6*, 2313−2317.

(13) Cao, J.; Ertekin, E.; Srinivasan, V.; Fan, W.; Huang, S.; Zhen, H.; Yim, J. W. L.; Khanal, D. R.; Ogletree, D. F.; Grossman, J. C.; Wu, J. *Nat. Nanotechnol.* **2009**, *4*, 732−737.

(14) Lee, S.; Cheng, C.; Guo, H.; Hippalgaonkar, K.; Wang, K.; Suh, J.; Liu, K.; Wu, J. *J. Am. Chem. Soc.* **2013**, *135*, 4850−4855.

(15) Eyert, V. *Ann. Phys.* **2002**, *11*, 650−702.

(16) Cao, J.; Fan, W.; Zheng, H.; Wu, J. *Nano Lett.* **2009**, *9*, 4001−4006.

(17) Fu, D.; Liu, K.; Tao, T.; Lo, K.; Cheng, C.; Liu, B.; Zhang, R.; Bechtel, H. A.; Wu, J. *J. Appl. Phys.* **2013**, *113*, 043707.

(18) Guiton, B. S.; Gu, Q.; Prieto, A. L.; Gudiksen, M. S.; Park, H. *J. Am. Chem. Soc.* **2005**, *127*, 498−499.

(19) Mayer, P. M.; Luerssen, D.; Ram, R. J.; Hudgings, J. A. *J. Opt. Soc. Am. A* **2007**, *24*, 1156.

(20) Farzaneh, M.; Maize, K.; Luerssen, D.; Summers, J. A.; Mayer, P. M.; Raad, P. E.; Pipe, K. P.; Shakouri, A.; Hudgings, J. A. *J. Phys. D: Appl. Phys.* **2009**, *42*, 143001.

(21) Komarov, P. L.; Burzo, M. G.; Raad, P. E. A Thermoreflectance Thermography System for Measuring the Transient Surface Temperature Field of Activated Electronic Devices. *Proceedings of 22nd IEEE SEMI-THERM Symposium*, Dallas, TX, 2006; pp 199−203.

(22) Gu, Q.; Falk, A.; Wu, J.; Ouyang, L.; Park, H. *Nano Lett.* **2007**, *7*, 363−366.

(23) Vermeersch, B.; Shakouri, A. Simultaneous Thermal Imaging of Peltier and Joule Effects. *IMAPS Thermal ATW*, Palo Alto, CA, 2010

(24) Grauby, S.; Forget, B. C.; Hole, S.; Fournier, D. *Rev. Sci. Instrum.* **1999**, *70*, 3603.

(25) Marini, C.; Arcangeletti, E.; Di Castro, D.; Baldassare, L.; Perucchi, A.; Lupi, S.; Malavasi, L.; Boeri, L.; Pomjakushina, E.; Conder, K.; Postorino, P. *Phys. Rev. B* **2008**, *77*, 235111.

(26) Tselev, A.; Luk'yanchuk, I. A.; Ivanov, I. N.; Budai, J. D.; Tischler, J. Z.; Strelcov, E.; Kolmakov, A.; Kalinin, S. V. *Nano Lett.* **2010**, *10*, 4409−4416.

(27) Miller, C.; Triplett, M.; Lammatao, J.; Suh, J.; Fu, D.; Wu, J.; Yu, D. *Phys. Rev. B* **2012**, *85*, 085111.

(28) Oh, D. W.; Ko, C.; Ramanathan, S.; Cahill, D. G. *Appl. Phys. Lett.* **2010**, *96*, 151906.

(29) Strelcov, E.; Tselev, A.; Ivanov, I.; Budai, J. D.; Zhang, J.; Teschler, J. Z.; Kravchenko, I.; Kalinin, S. V.; Kolmakov, A. *Nano Lett.* **2012**, *12*, 6198−6205.

(30) Khachaturyan, A. G. *Theory of the Structural Transformation in Solids*; Dover Publications: New York, 1983.

(31) Gu, Y.; Cao, J.; Wu, J.; Chen, L. *J. Appl. Phys.* **2010**, *108*, 083517.

(32) Wei, J.; Wang, Z. H.; Chen, W.; Cobden, D. H. *Nat. Nanotechnol.* **2009**, *4*, 420−424.

(33) Cao, J.; Fan, W.; Chen, K.; Tamura, N.; Kunz, M.; Eyert, V.; Wu, J. *Phys. Rev. B* **2010**, *82*, 241101.

Supporting Information for:

Direct observation of nanoscale Peltier and Joule effects at metal-insulator domain walls in vanadium dioxide nanobeams

Tela Favaloro[1,2†], Joonki Suh[3†], Bjorn Vermeersch[2], Kai Liu[4], Yijia Gu[5], Long-Qing Chen[5], Kevin X. Wang[3], Junqiao Wu[3,4], Ali Shakouri[1,2]*

[1]Baskin School of Engineering, University of California, Santa Cruz, CA 95064, USA

[2]Birck Nanotechnology Center, Purdue University, West Lafayette, IN 47907, USA

[3]Department of Materials Science and Engineering, University of California, Berkeley, CA 94720, USA

[4]Materials Sciences Division, Lawrence Berkeley National Laboratory, Berkeley, CA 94720, USA

[5]Deparment of Materials Sciences and Engineering, Pennsylvania State University, University Park, PA 16802, USA

* Corresponding authors: shakouri@purdue.edu

1. CCD based thermoreflectance thermal imaging
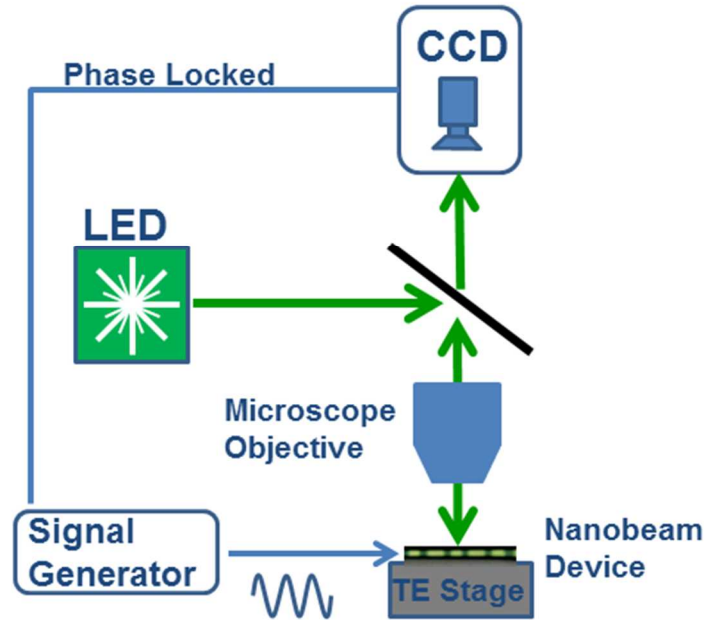
Figure S1. Schematic of the general experimental setup for thermoreflectance imaging.

The basic thermoreflectance principle used for these measurements is as follows (Fig. S1): Light is emitted from the LED to the beam splitter and is focused on the device-under-test (DUT) through a microscope objective. The DUT is under constant illumination for the duration of the experiment. A non-offset sinusoidal voltage is applied to the DUT (Fig. S2 upper) to create an oscillating temperature field (Fig. S2 center) comprised of Peltier and Joule signals. The change in temperature relative to the ambient is detected by the CCD camera as an alteration in the reflected light. The CCD is phase locked with the reflected signal, operating at eight times the frequency of the bias signal. In this way, eight images are used to reconstruct a single excitation

cycle. We represent each eighth-period integral of the oscillating reflectivity field with the notation B_n, where n=1…8 (Fig. S2 lower). Averaging over many cycles reduces the signal to noise ratios of this lock-in technique.
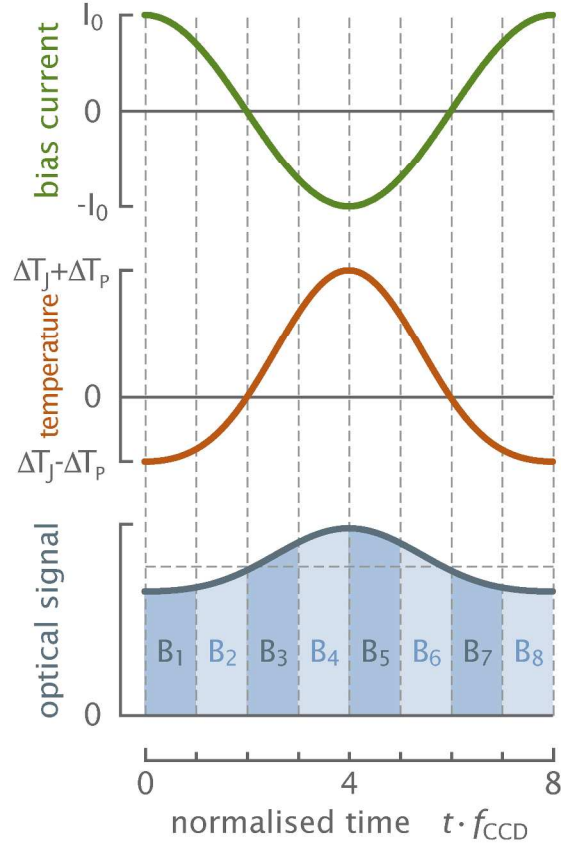
Figure S2. Schematic of principle of bi-polar thermoreflectance technique.

The magnitude of the temperature changes relative to the ambient due to thermoelectric effects are defined as:

$$|\Delta T_P| = \frac{|\Delta R_P|}{C_{TR} \cdot R_0} \qquad\qquad |\Delta T_J| = \frac{|\Delta R_J|}{C_{TR} \cdot R_0}$$

where R_0 refers to the baseline reflectivity field and is the sum of the eight images that comprise a full period, as the transient components cancel. C_{TR} is the thermoreflectance coefficient. The

Peltier (subscript P) and Joule (subscript J) effects manifest at the first and second harmonics of the bias signal, respectively. Thus, the respective reflectivity variations are:

$$|\Delta R_P| = \frac{\pi}{\sqrt{2}\sqrt{2-\sqrt{2}}}\sqrt{(B_1-B_5)^2+(B_2-B_6)^2+(B_3-B_7)^2+(B_4-B_8)^2}$$

$$|\Delta R_J| = \frac{2\pi}{\sqrt{2}}\sqrt{(B_1+B_5-B_3-B_7)^2+(B_2+B_6-B_4-B_8)^2}$$

The relative phase information (φ) for the respective temperature fields at each harmonic can be reconstructed as:

$$\tan(\varphi_P) = -\frac{B_1+B_2+B_3+B_4-B_5-B_6-B_7-B_8}{B_1+B_2-B_3-B_4-B_5-B_6+B_7+B_8}$$

$$\tan(\varphi_J) = -\frac{B_1+B_2-B_3-B_4+B_5+B_6-B_7-B_8}{B_1-B_2-B_3+B_4-B_5-B_6-B_7+B_8}$$

2. Theoretical calculation of domain wall angles

For coherent interfaces, the domain wall orientation is determined by the elastic energy. According to Khachaturyan's microelasticity theory, the elastic energy of a single coherent inclusion in the matrix of the parent phase can be written as

$$F_{Elastic} = \frac{1}{2}\iiint \frac{d^3k}{(2\pi)^3}\mathbf{B}(\mathbf{n})\left|\rho(\mathbf{k})\right|^2 \tag{S1}$$

where $\rho(\mathbf{k})$ is the Fourier transform of the shape function of an arbitrarily shaped coherent inclusion and

$$\mathbf{B}(\mathbf{n}) = \lambda_{ijkl}\varepsilon_{ij}^0\varepsilon_{kl}^0 - n_i\sigma_{ij}^0\mathbf{\Omega}_{jl}(\mathbf{n})\sigma_{lm}^0 n_m \tag{S2}$$

is the function of elastic energy density in the direction $\mathbf{n}=\mathbf{k}/k$. λ_{ijkl} is the elastic stiffness tensor and ε_{ij}^0 is the stress-free transformation strain (eigenstrain); the stress-free transformation stress (eigenstress) is given as

$$\sigma_{ij}^0 = \lambda_{ijkl}\varepsilon_{kl}^0. \tag{S3}$$

$\Omega_{ij}(\mathbf{n})$ is the inverse tensor such that

$$\Omega_{ij}^{-1}(\mathbf{n}) = \lambda_{iklj}n_k n_l. \tag{S4}$$

All indices run from 1 to 3. The Einstein summation is used. By minimizing $\mathbf{B(n)}$, we can find the domain wall configuration with the minimum elastic energy, or the so-called habit plane.

The structural phase transitions for both the M_R/I_{M1} and the M_R/I_{M2} coexisting states each have four variants characterized by different stress-free transformation strains. Due to the lack of anisotropic elastic constants for the material system, we used the experimentally measured Young's modulus of 140 GPa and took Poisson's ratio to be 0.35. For each eigenstrain variant, we calculated all the possible habit planes for both M_R/I_{M1} and M_R/I_{M2} by minimizing Equation (S2).

Table S1 lists all the possible habit planes for M_R/I_{M1} interface. The planes of M_R/I_{M1} can be divided into two groups according to the possible values of angles θ and φ (as defined in Figure S3): planes with angle θ of 56° (a, c, e and g) and those at an angle of 21° (b, d, f and h). All these plane orientations have identical elastic energy density, i.e. $B(\mathbf{n}) = 1.489 \times 10^7$ J/m^3. Assuming all domain walls have the same width, the total elastic energy of each domain wall is proportional to its wall area. As shown in Table S1, the planes with angle $\theta = 56°$ have smaller wall area, assuming a square NB cross-section. Consequently, these plane orientations have lower elastic energy and thus are favored. The possible habit planes for M_R/I_{M2} domain walls are

listed in Table S2. Similarly, the planes of M_R/I_{M2} can also be divided into two groups: planes with angle θ of 89° (a, b, e and f) and those at an angle of 33° (c, d, g and h). The elastic energy density of M_R/I_{M2} domain walls, $B(\mathbf{n}) = 4.364 \times 10^7$ J/m³, is higher than that of M_R/I_{M1} due to the different eigenstrain imposed by the lattice. However, all possible plane configurations have the same wall area and are equivalent if only elastic energy is considered. Anisotropic gradient energy coefficient, anisotropic elastic modulus and different beam geometries may favor one type of the listed plane configurations. Nevertheless, the domain wall angle θ is the fingerprint of the wall type, i.e. 56° (or experimentally observed 48-52°) for M_R/I_{M1} and 89° (or experimental observed 90°) for M_R/I_{M2}.
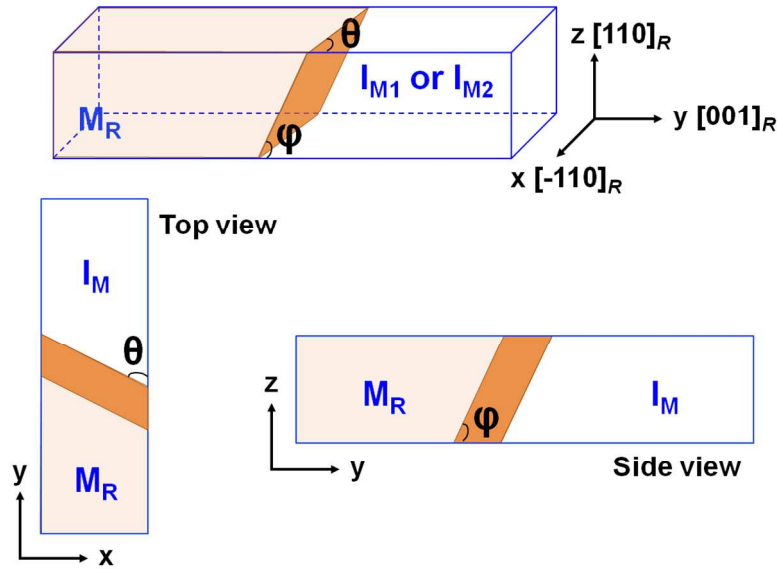
Figure S3. Schematic of the M_R/I_M domain walls. The angle θ represents the acute angle between the intersection on the top surface and the side plane. This angle is what is observable in the experiment. The angle φ represents the acute angle between the intersection on the side wall and the bottom/top surface.

3. Domain wall propagation
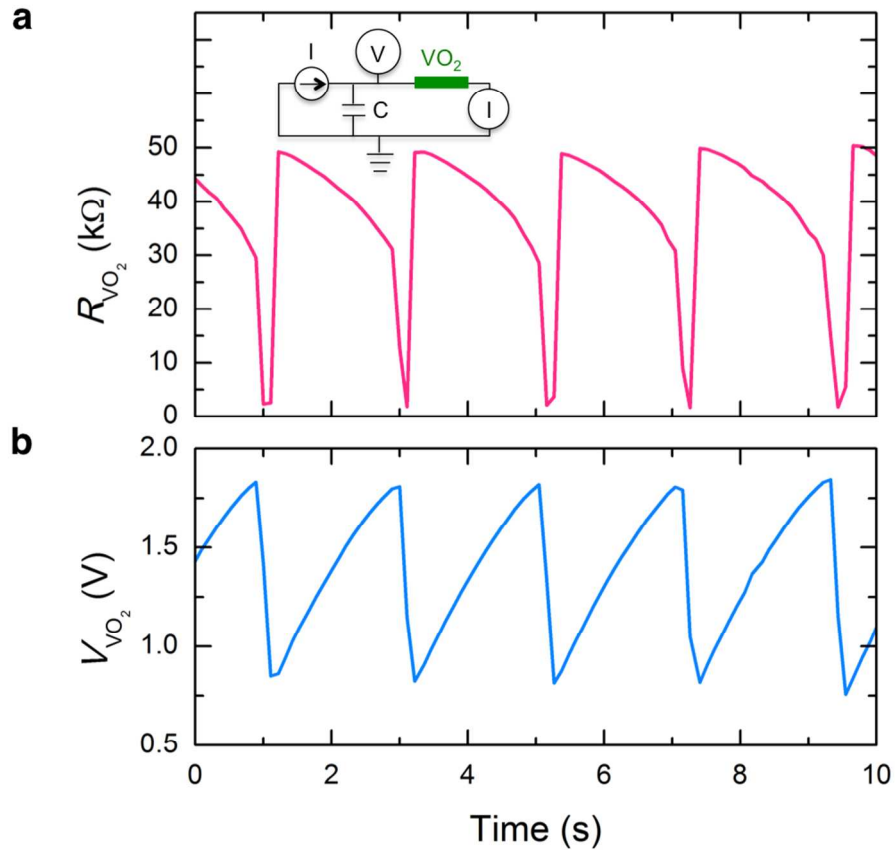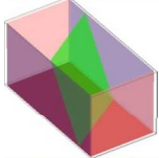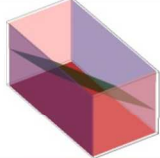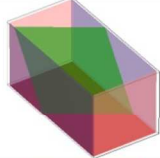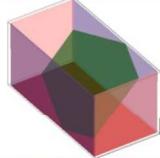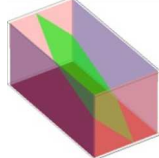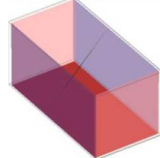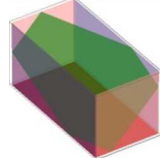
Figure S4. Resistance (**a**) and voltage (**b**) oscillation induced by localized Peltier and Joule activities at M-I interfaces. **Inset.** Circuit used to control the phase oscillation.

Junction electro-thermal effects induce M-I domain walls to propagate along a VO_2 NB and can be regulated through the charging and discharging processes of a capacitor connected in parallel in the circuit (Fig. S4a inset). Figure S4 shows the oscillating resistance and voltage of a VO_2 NB as a function of time when a constant DC current (~ 90 μA) is applied and a shunt capacitor (~ 100 μF) is used. The stationary M-I domain walls, stabilized at 353 K, start to move when the locally generated Peltier and Joule effects are sufficiently strong to trigger MIT along the VO_2 NB. The M_R domain gradually grows as heat accumulates from the applied current and

an immediate drop in R_{VO_2} as well as V_{VO_2} is observed as the NB transits into a homogeneous metallic state. This provides a low-resistance current pathway through the VO$_2$ NB, thus discharging the capacitor rapidly. As I_{VO_2} decreases during capacitor discharge, the NB cools sufficiently to regenerate the M-I configuration accompanied by an abrupt increase of R_{VO_2}. Further functionality may be achieved with better control of the domain drift by tuning parameters such as substrate adhesion, shunt capacitance, the applied current and ambient temperature, etc. We would like to highlight that domain wall movement was observed at large current densities (>60-90μA). At the lower current amplitudes where thermoreflectance imaging was performed, we did not observe significant domain movement during the measurement. However, highly localized electro-thermal activity at the domain walls was detected which is a driving force for the phase change in VO$_2$ and thus wall propagation along the nanobeam.
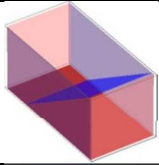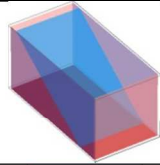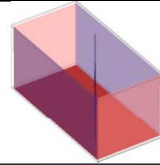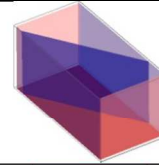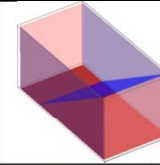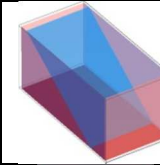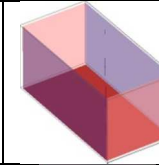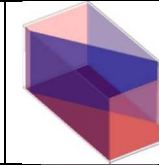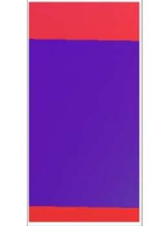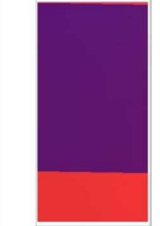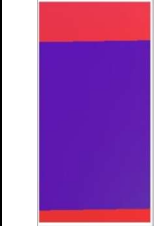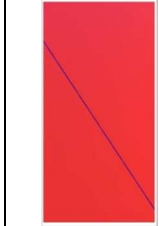
Table S1. Domain wall types of M_R/I_{M1}

M_R/I_{M1}	a	b	c	d	e	f	g	h
3D plot								
Top view								
Side view								
θ	56.0	21.4	56.0	21.4	56.0	21.4	56.0	21.4
φ	56.0	21.4	56.0	21.4	56.0	21.4	56.0	21.4
Area*	$1.38\ a^2$	$3.74\ a^2$	$1.38\ a^2$	$3.74\ a^2$	$1.38\ a^2$	$3.74\ a^2$	$1.38\ a^2$	$3.74a^2$

The green planes represent the domain walls of M_R/I_{M1}

* The shape of the cross-section of the NB is assumed to be square with length a. Therefore, the cross-sectional area of the NB is a^2. All angles are presented in degrees.

Table S2. Domain wall types of M_R/I_{M2}

M_R/I_{M2}	a	b	c	d	e	f	g	h
3D plot								
Top view								
Side view								
θ	89.0	89.0	33.3	33.3	89.0	89.0	33.3	33.3
φ	33.3	33.3	89.0	89.0	33.3	33.3	89.0	89.0
Area*	$1.82\,a^2$	$1.82\,a^2$	$1.82\,a^2$	$1.82\,a^2$	$1.82\,a^2$	$1.82\,a^2$	$1.82\,a^2$	$1.82a^2$

The blue planes represent the domain walls of M_R/I_{M2}

* The shape of the cross-section of the NB is assumed to be square with length a. Therefore, the cross-sectional area of the NB is a^2. All angles are presented in degrees.